

Electrodeposition of Tin and Antimony-Based Anode Materials for Sodium-Ion Batteries

To cite this article: Jessica R. Gallawa et al 2024 J. Electrochem. Soc. 171 040524

View the article online for updates and enhancements.

You may also like

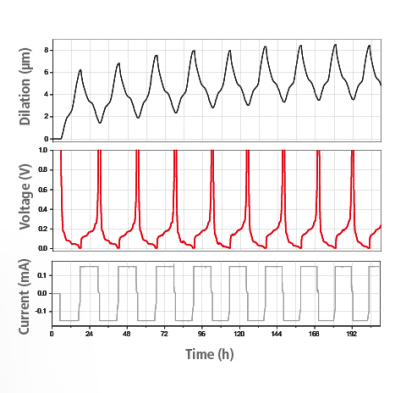
- Effects of bi-dopants Ni and Fe on tin antimonide alloy anodes: physico and electrochemical studies
 D Lakshmi, B Nalini, S Jayapandi et al.
- D Laksiiiii, D Naiiiii, O Jayapandi et al.
- Study on the effect of tin and antimony oxide interlayer on the performance of titanium-based manganese dioxide anode Bo-Yan Du, San-Fan Wang and Sheng-San Yu
- Compound semiconducting SnSb alloy anodes for Li ion batteries: effect of elemental composition of Sn—Sb Lakshmi D, Jayapandi S, Nalini B et al.

Watch Your Electrodes Breathe!

Measure the Electrode Expansion in the Nanometer Range with the ECD-4-nano.

- ✓ Battery Test Cell for Dilatometric Analysis (Expansion of Electrodes)
- ✓ Capacitive Displacement Sensor (Range 250 μm, Resolution ≤ 5 nm)
- ✓ Detect Thickness Changes of the Individual Half Cell or the Full Cell
- ✓ Additional Gas Pressure (0 to 3 bar) and Temperature Sensor (-20 to 80° C)





See Sample Test Results:



Download the Data Sheet (PDF):



Or contact us directly:

- +49 40 79012-734
- www.el-cell.com





Electrodeposition of Tin and Antimony-Based Anode Materials for Sodium-Ion Batteries

Jessica R. Gallawa, Deffrey Ma, and Amy L. Prieto Defrey Ma, and Defrey Ma, a

Department of Chemistry, Colorado State University, Ft. Collins, Colorado 80523-1872, United States of America

Tin antimonide (SnSb) is a promising alloying anode for sodium-ion batteries due to its high theoretical capacity and relative stability. The material is popular in the battery field, but, to our knowledge, few studies have been conducted on the influence of altering Sn and Sb stoichiometry on anode capacity retention and efficiency over time. Here, Sn-Sb electrodes were synthesized with compositional control by optimizing electrodeposition parameters and stoichiometry in solution and the alloys were cycled in sodium-ion half-cells to investigate the effects of stoichiometry on both performance and electrochemical phenomena. Higher concentrations of antimony deposited into the films were found to best maintain specific capacity over 270 cycles in the tinantimony alloys, with each cell showing a slow, gradual decrease in capacity. We identified that a 1:3 ratio of Sn:Sb retained a specific capacity of 486 mAh g⁻¹ after 270 cycles, highlighting a need to explore this material further. These results demonstrate how control over stoichiometry in Sn-Sb electrodes is a viable method for tuning performance.

© 2024 The Electrochemical Society ("ECS"). Published on behalf of ECS by IOP Publishing Limited. [DOI: 10.1149/1945-7111/ad3854]

Manuscript submitted November 16, 2023; revised manuscript received March 11, 2024. Published April 16, 2024.

Supplementary material for this article is available online

The economic and ecological push for renewable energy production presents a challenge in developing grid storage technology. Large-scale electrochemical storage is required for grid-level energy storage, and rechargeable batteries are an attractive avenue for short-term energy storage. The dominant battery technology, the lithiumion battery (LIB), is unable to fully address this issue due to the scarcity of lithium. A sodium-ion battery (NIB) uses the same working principle as LIBs but utilizes Earth-abundant, low-cost sodium compounds instead of lithium compounds. However, as they differ in their charge carrier, the components that operate in LIBs are not functional for NIBs. The most common LIB anode, graphite, presents challenges for NIBs as the relative atomic size of sodium inhibits complete intercalation. Exploring compatible anode materials for NIBs is necessary for their viability in the current and future markets.

As an alternative to intercalation anodes, alloying anode materials are promising with competitive theoretical capacities for NIBs. $^{4.5}$ Sn and Sb are both individually attractive alloying anode materials due to their high theoretical capacities with sodium (847 mAh g $^{-1}$ and 660 mAh g $^{-1}$ from the formation of Na $_{3.75}$ Sn and Na $_{3}$ Sb, respectively, Scheme 1). However, issues arise in alloying anodes from their high-volume expansion during sodiation (420% for Sn and 380% for Sb, for instance). To become viable anode materials, the volume expansion experienced by alloying anodes during cycling must be accommodated. Here, we study tin antimonide (SnSb) as an anode of interest due to its high theoretical capacity (742 mAh g $^{-1}$) and stability.

$$SnSb + 6.75Na^{+} + 6.75e^{-} \xrightarrow[\text{desodiation}]{\text{solitation}} Na_{3}Sb + Na_{3,75}Sn$$

Together, Sn and Sb have been shown to increase the overall cycle lifetimes of NIBs when compared to Sn or Sb alone. Because of these qualities, other groups have successfully synthesized tin and antimony-based anodes for battery applications. Sputtering, bulk synthesis methods, and nanoparticle methods have been successfully employed in a number of studies. An example of a microscale synthesis was described by Yi et al., who synthesized hollow Sn-Sb spheres with a displacement reaction between Sn powder and SbCl₃ dissolved in ethanol. There have also been a number of studies that utilize carbonaceous species in conjunction with tin antimonide through ball milling, electrospinning, template-assisted freeze

drying, and carbothermal reduction. ^{10–19,23} The main drawback to this type of synthesis is that it introduces binders and a degree of inhomogeneity that is not optimal for fundamental studies. ²⁴ Finally, many groups have used DC and/or RF magnetron sputtering to create films with control over stoichiometry. ^{9,20–22} While there have been many reported synthesis pathways for tin antimonide based anode materials, we chose to investigate an electrodeposition-based synthesis, as this method is scalable, reproducible, and does not depend on the introduction of carbonaceous binders. ^{24,25}

Previously, our group developed an electrodeposition solution for the electrochemical deposition of SnSb. ²⁶ Upon exploring this synthesis further, we found that several variables are quite sensitive. Specifically, we found that films were forming sparse, uneven deposits in quantities much smaller than anticipated with the solution parameters outlined in the work above. To combat this, we sought to systematically evaluate the synthesis to identify variables that could lead to problems. After re-evaluating our synthesis methods, we found that the solution was sensitive to a number of variables, including deposition temperature, water incorporation, and the chosen reference electrode. To understand why the synthesis was not behaving similarly to previous studies, we started with the solvent used, a deep eutectic solvent.

Deep eutectic solvents (DES) are regarded as an ionic liquid analog for their similar conductive properties and tunable chemistry.²⁷ The deep eutectic solvent used in this work, ethaline, is a DES which is formed from the combination and complexation of quaternary ammonium salts (choline chloride in this work) with hydrogen bond donors (ethylene glycol in this work). The complexation creates an equilibrium where the chloride is dissociated from the ammonium, creating a highly conductive solvent with a large electrochemical window.²⁸ Because of the anhydrous nature of the solvent, electrodepositions can proceed at larger potentials than in aqueous systems without concern for H2 gas evolution and subsequent passivation of the surface with oxides and hydroxides.²⁹ Despite these advantages, the viscosity of ethaline remains an issue regarding electrodeposition.³⁰ At room temperature, ethaline exhibits roughly 40-80 cP,³¹ while aqueous electrodeposition baths without bulky organic additives tend to have viscosity values <1 cP.³² Abbott et al. identified an inverse correlation in ionic conductivity of several DES, including ethaline, based on the viscosity of the solution.³⁰ We hypothesized that the viscosity was likely inhibiting electrodeposition, so our synthetic strategy started with exploring methods to increase the ionic conductivity of the dissolved metal ions. 26,33,34

Herein, we report optimizing SnSb thin film materials via compositionally controlled electrodeposition. Our results are

Scheme 1. The theoretical overall reaction of SnSb with sodium.

applicable to a wide range of the SnSb phase space through stoichiometric control of the SnSb electrodeposition solution. We sought to optimize the electrodeposition of crystalline SnSb by increasing temperature, monitoring stir rate, and minimizing water incorporation. Once synthesis parameters were established, we investigated the effects of solution stoichiometry on film composition and morphology, and electrochemical cycling studies were conducted to identify optimal stoichiometries for Sn and Sb in a NIB system (Fig. 1).

Experimental

Synthesis of ethaline deposition solution.—All glassware involved in synthesis was oven-dried overnight. Choline chloride (Acros Organics, 99%) was recrystallized in absolute ethanol, vacuum filtered, then left in a vacuum oven at 110 °C overnight. Water was distilled off ethylene glycol (Fisher Scientific, 99.8%) in a simple distillation apparatus. Ethylene glycol and choline chloride were combined in a 2:1 molar ratio, respectively. The solution was mixed at 80 °C for 3−6 h while vigorously stirring. Antimony (III) chloride (SbCl₃, Sigma Aldrich, ≥99.0%, 50 mM) and tin (II) chloride dihydrate (SnCl₂*2H₂O, Sigma Aldrich, 98%, 50 mM) were added to the ethaline solution and heated at 80 °C while vigorously stirring for roughly 20–30 min (until mostly dissolved)

then sonicated for 5 min to ensure dissolution. Solutions were used within one week of preparation and stored in a sealed container.

Electrodeposition parameters.—All electrochemical measurements of ethaline deposition solutions were performed using a Gamry Reference 3000 Potentiostat and analyzed using Gamry Analyst software. A water-circulating jacket beaker was used to bring the ethaline solution to 80 °C. Cyclic Voltammetry (CV) was performed using a three-electrode setup, with a platinum working electrode and platinum mesh counter electrode. Scans were conducted at 50 mV s⁻¹ and started at 0 V vs $Fe(CN)_6^{3-/4-}$ then proceeded to -1.25 V for the initial sweep, followed by a positive sweep to 1 V and finally a last sweep to return to 0 V.

The reference electrode was a homemade reference electrode following a previous synthesis. Briefly, the reference was made using a 2.5 mM potassium ferricyanide ($K_3Fe(CN)_6$, Fisher Scientific, 98%) combined with 2.5 mM potassium hexacyanoferrate (II) trihydrate ($K_4Fe(CN)_6*3H_2O$, Oakwood chemical, 98%) and dissolved in ethaline. Electrodepositions were performed using a single-step chronoamperogram for 60 s at -0.9 V vs $Fe(CN)_6^{3-/4}$ on a nickel substrate with an area of 3.00 cm² at 80 °C. A ½' stir bar was placed at the bottom of the 50 ml heating jacket for stirred electrodepositions. After the films were deposited, they were immediately removed from the electrodeposition solution and thoroughly rinsed with ethanol, water, and then ethanol.

Half-cell assembly and galvanostatic cycling.—All electrolyte preparation and half-cells were assembled in an argon glovebox (<1 ppm O₂) using a two-electrode Swagelok setup. Each

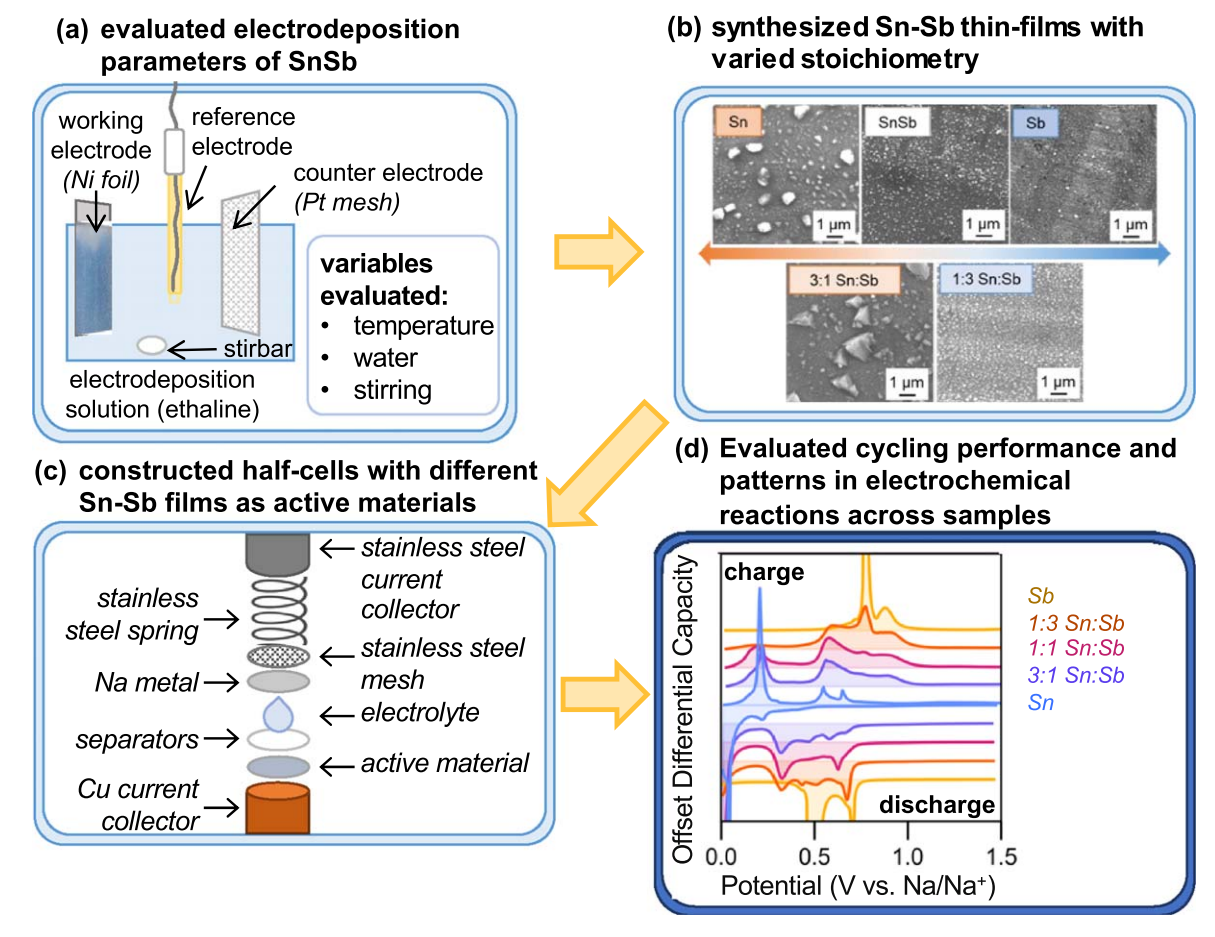


Figure 1. Summary of methods employed in the present study. Evaluated electrodeposition parameters of SnSb in Ethaline (a) including temperature, water incorporation, and stirring effects on thin film synthesis. Utilized SnSb synthesis parameters to electrodeposit varying compositions of Sn and Sb (b). Constructed half-cells using as-synthesized Sn-Sb thin films (c) and galvanostatically cycled half cells to evaluate cycling performance and electrochemical reactions across samples (d).

electrodeposited film was cut into a ½' diameter circle as the active material, and theoretical capacity was calculated using Faraday's law of electrolysis to calculate deposition mass. The cut thin film was then used as the working electrode, followed by a polypropylene separator (MTI Corp), then a Whatman glass filter paper, and another polypropylene separator. After this, $\sim\!20~\mu l$ of electrolyte was added, followed by a ½' punch of sodium metal polished with dry hexanes before use. The electrolyte consisted of a 1 M solution of sodium perchlorate (NaClO₄, Sigma-Aldrich, $>\!\!98\%$ ACS reagent) in propylene carbonate (PC, Sigma Aldrich, 99.7%) with a 5% addition by volume fluoroethylene carbonate (FEC, Sigma-Aldrich, 99%). Cells were allowed to rest for 12 h before cycling galvanostatically with an Arbin battery tester between 0.005 V and 1.5 V vs Na/Na $^+$ at a C/2 rate in room temperature (25 °C). C-rate was assigned based on the theoretical capacity of each anode.

Characterization.—The morphology of electrodeposited films was analyzed by Scanning Electron Microscopy (SEM) using a JEOL JSM-6500F Microscope at 15 kV, and Energy Dispersive X-ray Spectroscopy (EDS) with an Oxford instrument X-Max and Aztec Software. Crystalline phases were identified via Powder X-ray Diffraction (PXRD) using a Bruker D8 Discover DaVinci powder X-ray Diffractometer using Cu Kα radiation, and a 0.2 mm slit opening. X-ray Photoelectron Spectroscopy was performed with a Physical Electronics (PHI) 5800 series Multi-Technique ESCA system with a monochromatic Al Kα (hν = 1486.6 eV) X-ray source operating at 350.0 W.

For the compositional films (Sn, 1:3 Sn:Sb, SnSb, 3:1 Sn:Sb, and Sb), glancing angle X-ray diffraction was utilized on a Bruker D8 Discover Series II Thin Film Diffractometer using Cu K α radiation and a 0.100 mm detector slit opening. Theta values used were between 1 and 3°, which was decided by optimizing the signal from the [100] peak in Sn and the [101] plane in the remaining samples: Sn: 2.260° θ , 1:3 Sn:Sb: 2.114° θ , SnSb: 2.114° θ , 3:1 Sn:Sb: 1.538° θ , Sb: 1.987° θ . Rietveld refinements were carried out using TOPAS v6 software. Quantification of Sb and Sn atomic percentages were evaluated with Rietveld refinements in conjunction with elemental mapping via EDS. A detailed description of the refinements can be found in the SI (Supplementary Information, S10–14).

Results and Discussion

Evaluating electrodeposition parameters for SnSb.—Before evaluating the importance of specific synthetic variables of the deposition solution, we identified the redox phenomena of the electrodeposition bath using cyclic voltammetry. Cyclic voltammetry was used throughout this study to evaluate solution conditions between depositions. A representative cyclic voltammogram of Sn, Sb, and SnSb electrodeposition solutions are shown in Fig. 2 to illustrate (i) how we chose the potential at which we electrodeposited, and (ii) the redox phenomena we probed and how those correspond to tin and antimony salts in the solution. CVs for additional compositions of Sn-Sb electrodeposition solutions are shown in Fig. S1. For the cyclic voltammogram of the SnSb electrodeposition solutions, the reduction of Sb appears to be split into two peaks, which implies that the reduction from Sb(III) to Sb (0) occurs over multiple steps. The oxidation peaks at \sim -0.1 V vs $[Fe(CN)_6]^{3-/4-}$ for Sb also exhibit this feature, indicating separate oxidation steps. The peaks seen at higher potentials, based on compositional scans, were assigned as the conversion between Sb (III) and Sb(V), as well as the conversion between Sn(II) and Sn(IV) (Fig. 2). These preliminary scans were used to assign deposition potentials sufficiently past the reduction potential of Sn. Based on the peak reduction potential of Sn maximizing ~0.75 V vs $[Fe(CN)_6]^{3-/4-}$, a reduction potential of $-0.8 \text{ V vs} [Fe(CN)_6]^{3-/4-}$ was used for chronoamperometry. While this potential resulted in the deposited tin antimonide, surface coverage improved when the reduction potential was changed to -0.9 V vs $[\text{Fe}(\text{CN})_6]^{3-/4-}$.

Now that the cyclic voltammetry of tin and antimony salts have been introduced, the discussion will transition to changing synthetic variables to increase ionic conductivity. For context, Ma et al. 26 first studied the electrodeposition of SnSb from ethaline, but in attempting to reproduce this electrodeposition, no Sn or Sb species could be identified. Because of the increased viscosity exhibited in ethaline relative to aqueous electrodeposition solvents, the low ionic conductivity of metal salts was suspected to be inhibiting the electrodeposition of SnSb. To optimize the ionic conductivity for electrodeposition, we investigated water spiking, temperature, and stirring as variables as each of these methods increase the mobility of ions in solution.

The literature has mixed ideas on the influence of water incorporation in ethaline. 28,36,37 Brusas and Dela Pena studied the hygroscopicity of ethaline in atmospheric conditions and identified that over time, the electrochemical stability of ethaline decreased with water adsorption.³⁷ While water has been seen to reduce the electrochemical stability window of ethaline, one study by Alfurayi et al. investigated the influence of water spiking on the solution electrochemical stability window and solvation dynamics and found that the electrochemical stability window of ethaline does not change drastically with up to 10 wt% added water. 36 In fact, they found that solution viscosity increased, and solvation dynamics were enhanced with increasing amounts of water (below 10 wt% and above 1 wt%). To better understand how water would influence the electrodeposition of SnSb in our system, the concentration of added water in the electrodeposition solution was investigated as a method for lowering solution viscosity. Water spiking tests were performed, where pristine ethaline solutions were spiked with 0, 5, 10, 15, and 20 wt % water. Cyclic voltammetry was used to probe redox events in the solution as water was added (Fig. 3). As expected, the produced current of the reduction peaks at -0.3 and $-0.55 \,\mathrm{V}$ vs $[Fe(CN)_6]^{3-/4-}$ increased as the water was added due to the decrease in solution viscosity. Additionally, the reduction potential for Sn(II) and Sb(III) decreased in magnitude, indicating an increased electron transfer rate between the electrode and the solution. The integrated chronoamperometry of the SnSb samples electrodeposited from ethaline with water added show an increase in the charge passed with more significant amounts of water, which indicates increased mass transfer could be occurring.

While the addition of water appears to have increased the ionic conductivity throughout the solution, all SnSb samples deposited from ethaline spiked with water immediately became dendritic, as seen via qualitative "scratch testing" (rubbing the surface of the film and observing the amount of film disruption, Fig. S2) and with Scanning Electron Microscopy (SEM) images (Fig. 4). This resulted in crystalline SnSb (Fig. S3), but the dendritic morphology can be detrimental to film stability and robustness, and thus this method was not employed further to increase the overall ionic conductivity.

Next, we investigated elevated temperatures (above room temperature) as a parameter for increasing metal ionic conductivity during electrodeposition. Brusas et al. studied the effect of elevated temperatures on ethaline for extended periods of time and found that the optimal time to heat ethaline for full incorporation was between 3-9 h at 70.0 °C and that after 9 h the choline chloride crashed out of the solution.³⁷ The authors attributed this to a deviation from the eutectic phase brought on by evaporation of the ethylene glycol. Because of this limitation, all solutions were heated for no longer than 6 h so depositions could be carried out at elevated temperatures. Increasing the ethaline electrodeposition solution temperature did appear to increase diffusion as displayed in the increased peak current in the cyclic voltammetry studies (Fig. 5). Further diffusion studies of Sn and Sb in ethaline with temperature have revealed an increase in the diffusion coefficients of Sn and Sb, respectively, with increasing temperature (Figs. S4-S5) which help to explain why peak currents are increasing at greater temperatures. Chronoamperometry of the SnSb depositions were conducted (Fig. S6) which show increased charge passing with increased

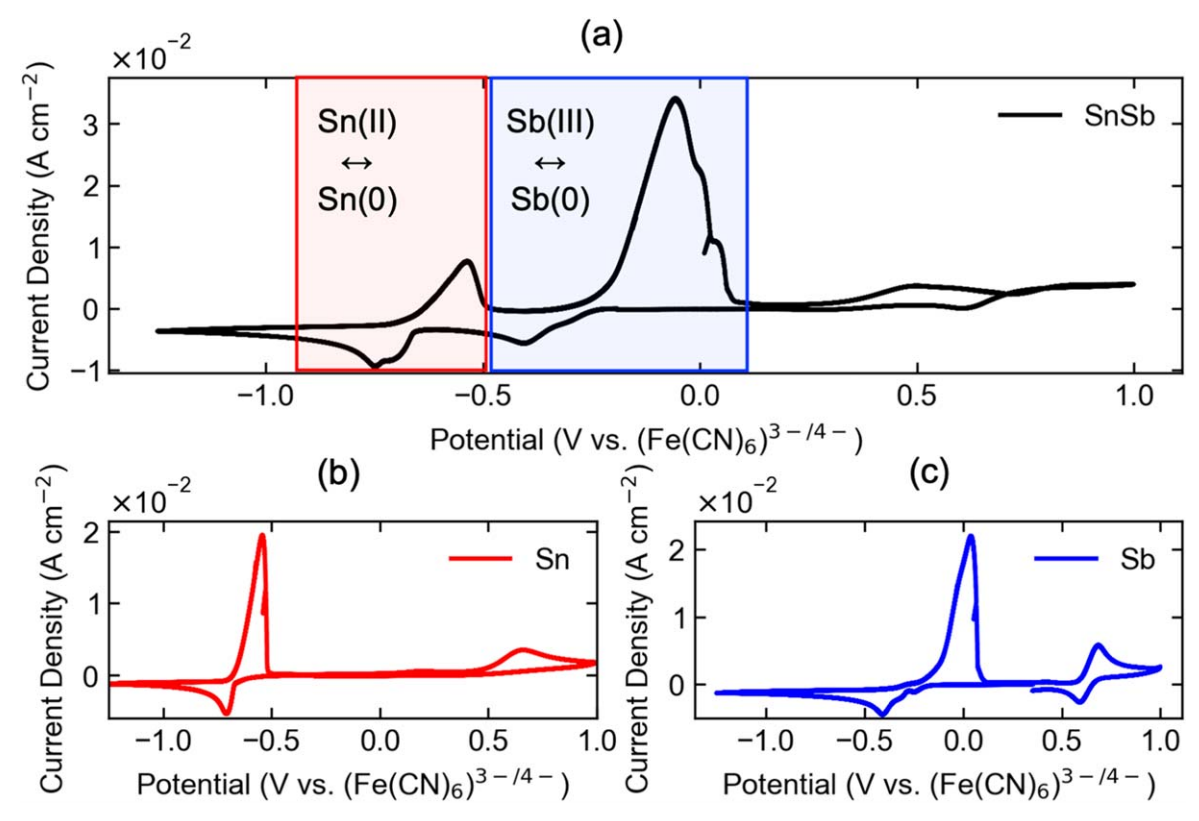


Figure 2. Cyclic voltammetry of (a) SnSb, (b) Sn, and (c) Sb electrodeposition solutions. SnSb solution consisted of 50 mM $SnCl_2*2H_2O$, 50 mM $SnCl_3*in$ ethaline. Sn solution consisted of 50 mM $SnCl_2*2H_2O$ in ethaline, Sb solution consisted of 50 mM $SnCl_3*in$ ethaline. Cyclic voltammetry was performed at 50.0 °C with a rate of 50 mV s⁻¹. Highlighted sections were added to emphasize redox chemistry. For both the Sn and SnSb electrodeposition solutions, a redox event is seen at ~ -0.55 V vs $(Fe(CN)_6)^{3-/4-}$ which corresponds to the Sn(0) and Sn(II) couple (highlighted in (a) in red). Around 0 V vs $(Fe(CN)_6)^{3-/4-}$ an Sb peak is evidenced with multiple overlaid redox peaks (highlighted in (a) in blue). Further positive $\sim 0.25-0.75$ V vs ref are Sn(II)/Sb(IV) and Sb(III)/Sb(V) peaks.

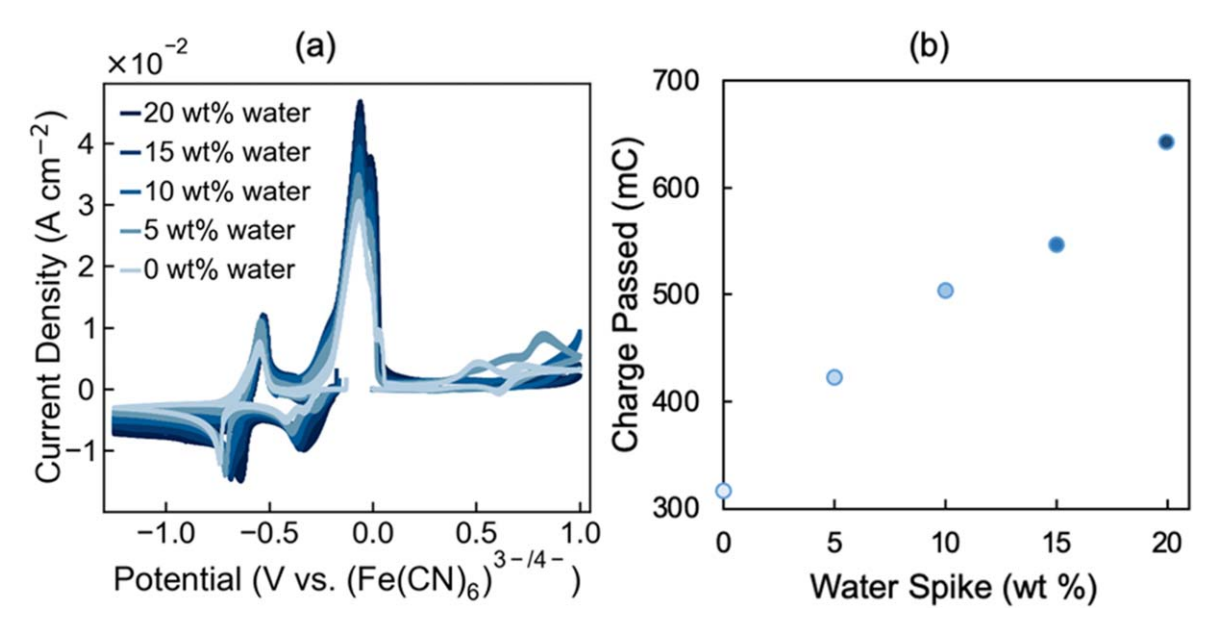


Figure 3. (a) Cyclic voltammetry of ethaline SnSb deposition solution with 0, 5, 10, 15, and 20 wt% water spiking in an ethaline with 50 mM SnCl₂*2H₂O and 50 mM SbCl₃, with a scan rate of 50 mV s⁻¹ at 50.0 °C. As water is added, the redox peaks increase in magnitude and shift to less negative potentials, indicating an increased rate of electron transfer between the electrode and the solution. (b) Integrated Chronoamperometry of ethaline SnSb deposition solution with 0, 5, 10, 15, and 20 wt% water spiking. Ethaline with 50 mM SnCl₂*2H₂O, 50 mM SbCl₃. Single-pulse chronoamperogram at -0.8 V vs [Fe(CN)₆]^{3-/4-} and 50.0 °C for 60 s. As water is added, the current passed during chronoamperometry increases, corresponding to an increase in ionic conductivity of the metals through the solution.

temperatures, indicating an increased rate of electron transfer in the solution, as seen with water spiking studies. Crystalline films of SnSb were formed for each of the electrodepositions between 50 $^{\circ}$ C

and 80 $^{\circ}$ C (Fig. S7), therefore increasing temperature was identified as a critical variable in increasing ionic conductivity of the electrodeposition solution.

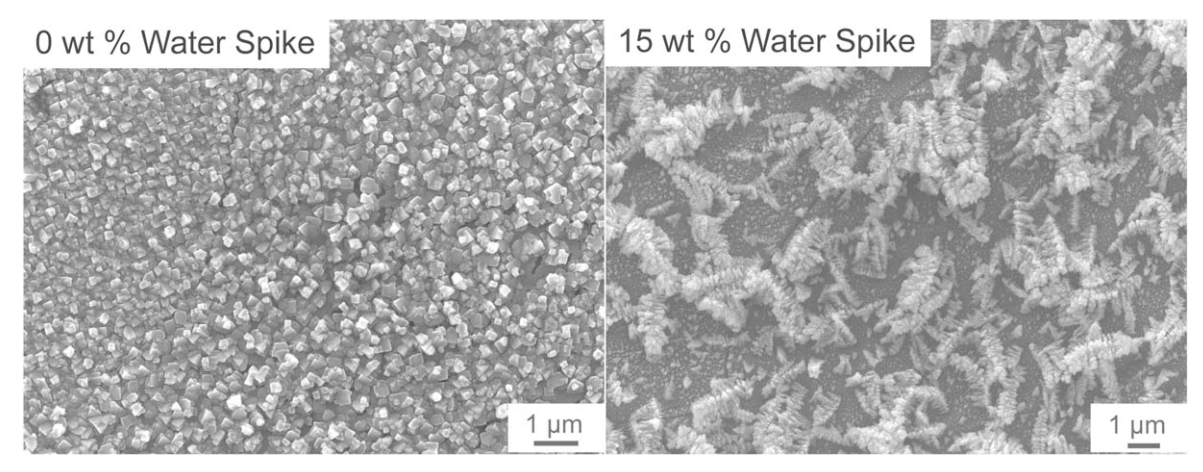


Figure 4. Comparison of morphological changes between SnSb electrodeposited from ethaline with 0 wt% water added (left) and 15 wt% water added (right) at 50.0 °C characterized with scanning electron microscopy (SEM). The SEM image of the SnSb film with 0 wt% water added shows homogenous coverage and morphology. The SEM image of tin antimonide film with 15 wt% water added exhibits large dendritic heterogeneous structures. Electrodeposited at -0.8 V vs $[\text{Fe}(\text{CN})_6]^{3-/4-}$, 50 °C for 60 s.

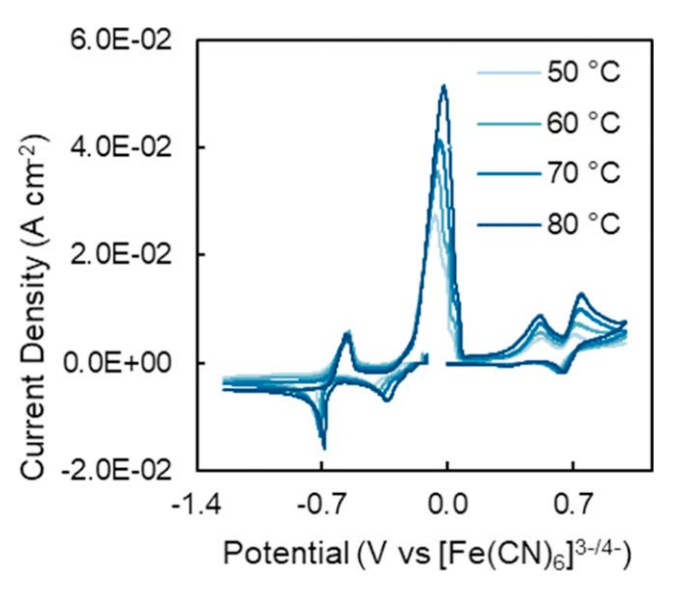


Figure 5. Cyclic voltammetry of ethaline SnSb deposition solution at 50.0, 60.0 70.0 and 80.0 °C with a blue hue gradient. Ethaline with 50 mM SnCl₂*2H₂O, 50 mM SbCl₃. Scan rate = 50 mV s⁻¹. Peak heights increased with elevated temperatures, indicating increased solution diffusivity.

The depositions described so far were all conducted with no stirring, so we sought to assist diffusion of bulk metals in solution by stirring the electrodeposition solution. While this method proved effective for the demonstrative purpose of increasing ionic mobility (Fig. S8), this method was not employed further to reduce variables which could be difficult to reproduce consistently (for instance, the shape of the stir bar, shape of the deposition container, distance between electrodes, stability of stir plate could change how the convection is exhibited at the electrode). Further studies with a rotating disk electrode could utilize convection more effectively.

In summary, we observed the effects temperature, water, and stirring, have on the electrodeposition of SnSb from ethaline. These variables were studied because of their potential to increase ionic conductivity. We found that spiking SnSb deposition solution with water lead to fragile, dendritic morphologies. We also identified that heating the ethaline deposition solution between 50 °C and 80 °C resulted in the electrodeposition of crystalline SnSb with homogeneity and even surface coverage. With an understanding of how to increase the ionic mobility of the electrodeposition solution, we next

sought to determine the effects of varying the Sn:Sb ratio on controlling thin film composition.

Studying the effect of bath stoichiometry on electrodeposition morphology and composition.—Changing the bath stoichiometry resulted in not only a variety in thin film compositions (where generally the stoichiometry of the film matched the starting ratio), but also resulted in varied morphologies across samples (Fig. 6). When comparing the morphology among the Sn-Sb films, a general trend was noted where grain sizes were much larger for samples containing Sn and gradually got smaller with increasing amounts of Sb. This is supported by the reported brightening effect ethaline has on Sb. The pure Sn sample exhibits large grains (ca. 0.5 μ m diameter) with inhomogeneous surface coverage. This has been identified by Brandão et al., who did an exploratory study on the electrodeposition of Sn from ethaline with and without carbon nanotubes. The start of the starting transfer of the starti

For the films with both Sn and Sb, stoichiometry was roughly quantified with elemental dispersive X-ray spectroscopy (EDS) and summarized in Table I. In the case of the films deposited from 3:1 Sn:Sb electrodeposition bath, a thin film with large, island-like crystals were observed with a rough stoichiometry of ~2.6 Sn:Sb, as well as a thin surface coating with faint Sn and Sb signals. A more detailed description of the quantification results from EDS can be found in the supporting information (Tables S1, S2, Fig. S9). The films electrodeposited from the 1:1 and the 1:3 Sn:Sb electrodeposition bath were more homogeneous, with EDS measuring relative stoichiometries as 1:1 and 1:2.3 Sn:Sb stoichiometry, respectively. With the crystal structures of both SnSb and Sb exhibiting rhombohedral symmetry, it is likely these form a solid solution of SnSb/Sb. To better understand the composition of these films, Rietveld refinements were pursued from X-ray diffraction (Fig. 7).

Rietveld refinements follow in line with the compositions identified in EDS mapping, and these compositions generally align with the bath stoichiometry (Table I). XRD identified mixed phases in the 1:3 Sn:Sb 3:1 Sn:Sb samples. For 1:3 Sn:Sb, an Sb phase and a $Sn_{0.25}Sb_{0.75}$ solid-solution phase was identified, whereas the 3:1 Sn: Sb film XRD identified a Sn and a $Sn_{0.6}Sb_{0.4}$ solid-solution phase. The presence of solid solutions, as well as the mixed phases of these Sn-Sb films, could influence how these materials operate as anode materials, so further work will need to be explored to deconvolute the respective roles of elemental composition, phase presence, and solid-solution formation on battery performance in Sn-Sb anodes.

Evaluation of Sn-Sb thin-films in Na-ion half-cells.—Once deposition parameters were established, the as-deposited SnSb and

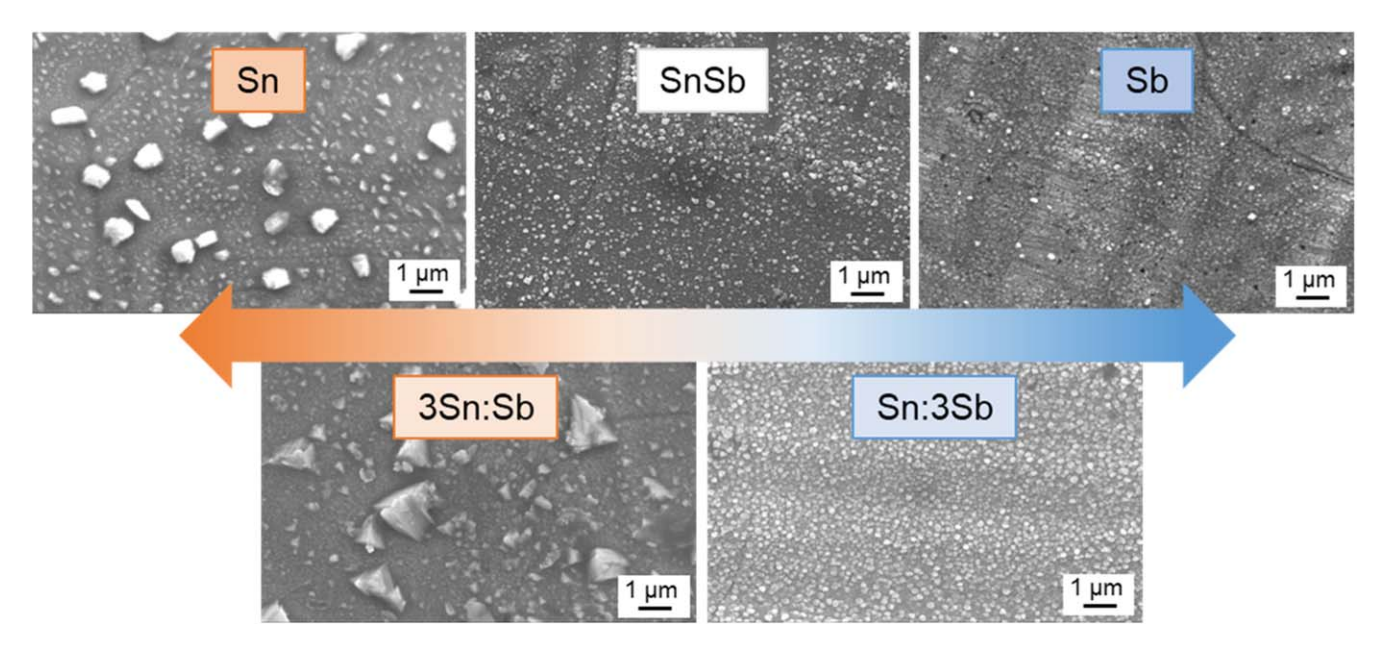


Figure 6. SEM images of films electrodeposited from ethaline baths with Sn, 3:1 Sn:Sb, SnSb, 1:3 Sn:Sb, and Sb stoichiometry. All images were taken at 9000X magnification, 10.0 mm working distance. Compositions are denoted as the composition of the deposition bath, as surface roughness, inhomogeneity, and solid solution presence impeded characterization of film stoichiometry. Sn and Sn-rich deposits exhibit large grains and uneven surface coverage, while Sb and Sb-rich films exhibit small grains. Detailed descriptions of elemental mapping via EDS is discussed in supplementary information (SI Table S1).

Nominal composition	Deposition bath stoichiometry	EDS atomic %	XRD phase %	Atomic % from XRD	Mass loading (mg/cm ²)
Sn	100% Sn	100% Sn	100% Sn	100% Sn	0.0317
3:1 Sn:Sb	75% Sn	72.6% Sn	49.1% Sn	80.3% Sn	0.109
	25% Sb	27.4% Sb	50.9% Sn _{0.6} Sb _{0.4}	19.7% Sb	
1:1 Sn:Sb	50% Sn	48% Sn	100% SnSb	50% Sn	0.100
	50% Sb	52% Sb		50% Sb	
1:3 Sn:Sb	25% Sn	30.3% Sn	28.4% Sb	17.7% Sn	0.0684
	75% Sb	69.7% Sb	71.6% Sn _{0.25} Sb _{0.75}	82.3% Sb	
Sb	100% Sb	100% Sb	100% Sb	100% Sb	0.0485

Sn-Sb thin films could be studied as anode materials in Na-ion batteries. To study the performance and lifetime of the compositions and identify trends between samples, compositionally controlled films were cycled in sodium-ion half-cells, meaning a 2-electrode cell with sodium metal as the counter electrode. This configuration was used to isolate electrochemical phenomena to the working electrode. Comparison between the differential capacity curves associated with each cell identified peaks correlating to cell death and solid electrolyte interphase (SEI) formation.

Table I. Massured stamic concentrations of an and sh from compositional complex

The Sn, 1:3 Sn:Sb, 1:1 Sn:Sb, 3:1 Sn:Sb, and Sb films were cycled at 0.5 C to study the lifetime of each film as an anode. Interestingly, the anode that observed the greatest capacity retention over 275 cycles (where one cycle is a galvanostatic charge and discharge between 0.01 and 1.5 V vs Na/Na⁺) was the 1:3 Sn:Sb film. Each alloy cell had a steady decline in capacity over the total lifetime, while the Sb barely approached a precipitous death during the final ~75 cycles (Fig. 8). For the films containing both Sn and Sb, the capacity retention over 275 cycles increased as more Sb was added. The increased capacity retention exhibited in Sb-containing anodes could be due to properties of the anode itself, for instance, how well the material adheres to the substrate, the grain size of the crystalline material, solid-state sodium diffusion mechanisms, or it could be from the presence of mixed phases between SnSb and Sb.

During battery cycling, electrolytes used in the battery tend to reduce at the surface of the anode, creating an interphase region between the anode and the electrolyte called the Solid Electrolyte Interphase (SEI). The SEI can provide a stable passivation layer between the electrode and electrolyte which inhibits further electrolyte reduction, but if the electrolyte is ill-suited for the anode material, the SEI that forms might not be passivating (leading to increased electrolyte reduction and often decreases in charge capacity), or it could inhibit the diffusion of sodium ions, which limits the power density of the battery. Sn alone performed poorly, which could indicate that the chosen electrolyte was ill-suited for Sn. These cells were cycled using a carbonate-based electrolyte, which has been shown to be detrimental to SEI formation in Sn anodes. ^{8,40} Further studies with X-ray photoelectron spectroscopy (XPS) will be pursued to deconvolute the role of SEI formation in the overall performance of the anode materials. However, for the presently studied system, the 1:3 Sn:Sb exhibited the greatest capacity retention over 275 cycles.

Differential capacity curves were conducted to identify theoretical sodiation and desodiation mechanisms of SnSb and to find correlations between electrochemical events and capacity fade. Differential capacity plots of Sn, 1:3 Sn:Sb, SnSb, 3:1 Sn:Sb, and Sb thin films were conducted to look for common patterns in capacity fade as well (Fig. S15). In particular, the mechanisms involved in sodiation and desodiation for the samples containing both Sn and Sb are of interest, as these will hopefully provide context for the increased capacity retention exhibited in the 1:3 Sn: Sb material. The differential capacity of the samples with both Sn and Sb reveals similar peak locations to that of SnSb, indicating that

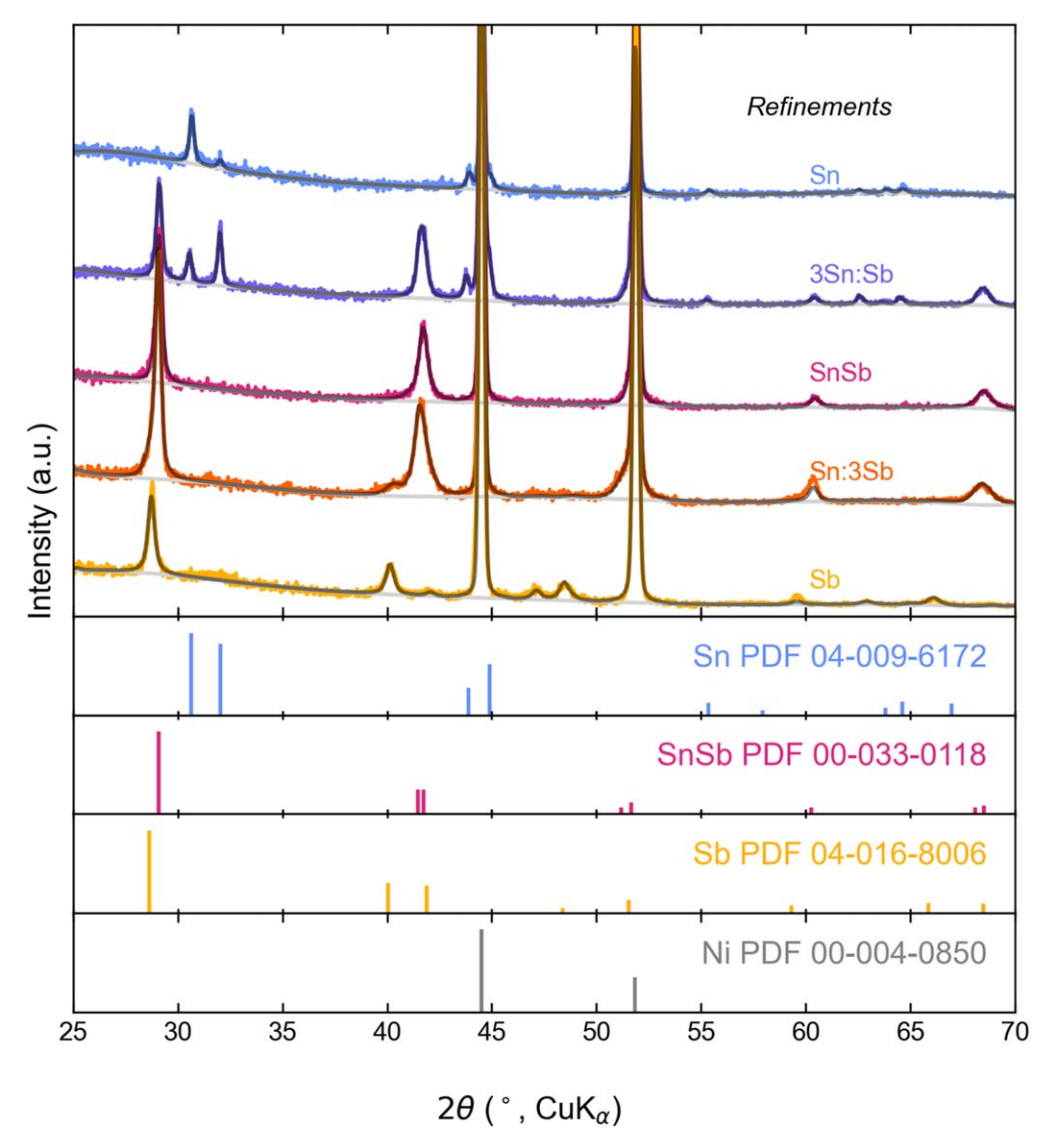


Figure 7. Glancing-Angle X-ray diffraction of Sn, 3Sn:Sb, SnSb, Sn:Sb, and Sb thin films. Black overlaid lines plotted are the fitting results after Rietveld refinements. Rwp values from Rietveld refinements: 6.35 for Sn, 7.86 for 3:1 Sn:Sb, 8.77 for SnSb, 9.62 for 1:3 Sn:Sb, and 10.21 for Sb. Further discussion of the refinements, along with quantification results, and difference curves, can be found in the supporting information (Supplementary Information, Figs. S10–S14).

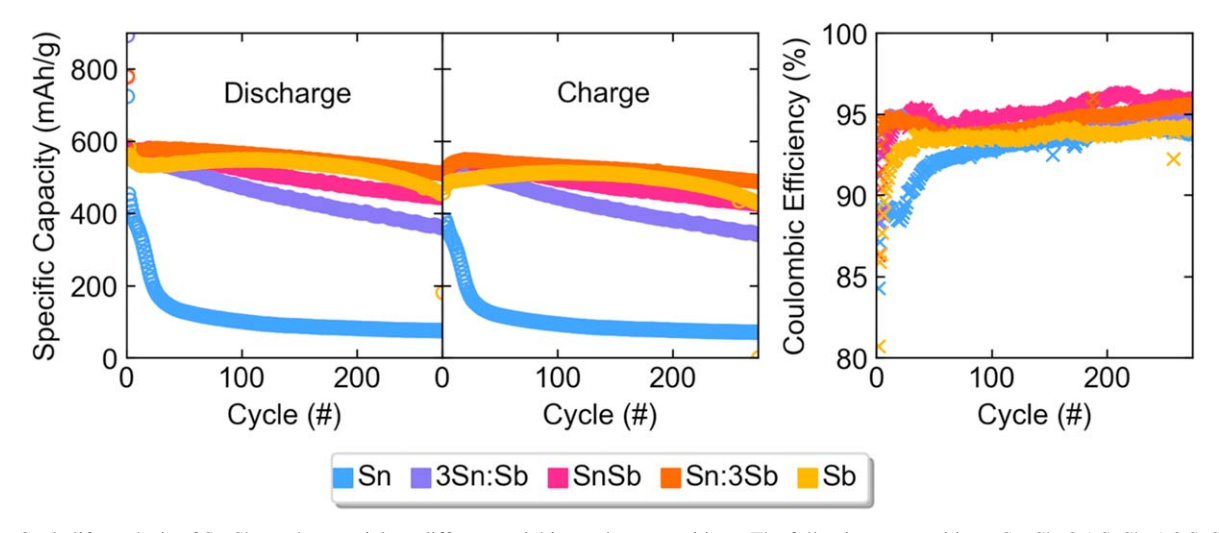


Figure 8. Cycle life analysis of Sn-Sb anode materials at different stoichiometric compositions. The following compositions, Sn, Sb, 3:1 SnSb, 1:3 SnSb and 1:1 SnSb, were cycled in a sodium half-cell at rate of C/2. In this analysis shaded in circles describe the charge capacity, outlined circles depict the discharge capacity, and x's correspond to the coulombic efficiency plotted against the y-axis on the right.

the mixed-phase samples undergo similar electrochemical phenomena (Fig. 9). The sodiation and desodiation mechanisms of SnSb are not yet fully understood, but there have been many different approaches to characterizing the intermediate phases seen in SnSb during cycling, for instance X-ray diffraction, transmission electron microscopy (TEM), X-ray absorption spectroscopy (XAS), Mössbauer spectroscopy, Scanning Electron Microscopy (SEM), and in situ Raman studies have each provided insight into this mechanism. $^{20-22,41,42}$ A generalized trend taken from the observed sodiation and desodiation transformations of SnSb is as follows. First, sodium reacts with Sb, creating a broad peak at \sim 0.7 V, and leaving an amorphous (a-) Sn phase:

$$SnSb + 3Na^{+} + 3e^{-} \rightarrow a - Sn + Na_{3}Sb$$
 [1]

At higher potentials, Sn is then sodiated to create an amorphous Na-Sn phase, resulting in a broad peak $\sim 0.5 \text{ V}$ vs Na/Na⁺. During the first cycle, there is a large peak at $\sim 0.5 \text{ V}$ vs Na/Na⁺, which we attributed to irreversible reduction of the electrolyte on the surface of the anode dwhich forms the Solid Electrolyte Interphase (SEI). This phase continues to sodiate until reaching a crystalline (c-) Na₁₅Sn₄ phase, resulting in a peak $\sim 0.3 \text{ V}$ vs Na/Na⁺:

$$Na_3Sb + a - Sn + xNa^+ + xe^- \rightarrow a - Na_xSn + Na_3Sb$$
 [2]

Where x is less than 3.7, and represents the stoichiometric amount of Na incorporated before achieving the crystalline (c-) Na₁₅Sn₄ phase:

$$a - \text{Na}_x \text{Sn} + (15 - x) \text{Na}^+$$

+ $(15 - x)e^- \rightarrow c - \text{Na}_{15} \text{Sn}_4 + \text{Na}_3 \text{Sb}$ [3]

There are reports indicating that Sn and Sb create a ternary phase during sodiation, however, the amorphous nature of the intermediate phases makes it difficult to identify.^{21,22}

Desodiation then starts by the desodiation of Sn, leaving behind an amorphous Sn phase, which would correspond to the two peaks at \sim 0.1–0.3 V vs Na/Na⁺, followed by two more peaks at \sim 0.5 and \sim 0.65 V vs Na/Na⁺:

$$c - \text{Na}_{15}\text{Sn}_4 + \text{Na}_3\text{Sb} \rightarrow a - \text{Sn}$$

+ $a - \text{Na}_x\text{Sn} + y\text{Na}^+ + ye^-$ [4]

$$Na_3Sb + a - Na_xSn \rightarrow a - Sn$$

+ Na_3Sb + xNa⁺ + xe⁻ [5]

And finally, the Sb phase is desodiated, leaving behind a partially reformed SnSb anode. 20 This process begins at $\sim\!0.6$ V vs Na/Na $^+$ in the Sb alone, creating a sharp peak followed by a shoulder. However, in the SnSb sample, this process is more convoluted with the Sn desodiation peaks, creating a broad set of overlapping peaks $\sim\!0.5\text{--}1.2$ V vs Na/Na $^+$:

$$a - \operatorname{Sn} + \operatorname{Na_3Sb} \to \operatorname{SnSb} + 3\operatorname{Na^+}$$
 [6]

In the case of 1:3 Sn:Sb and 3:1 Sn:Sb, the differential capacity plots exhibit similar structural features, indicating they go through similar transformations. One pattern seen across the samples with both Sn and Sb is that the sodiation and desodiation peaks $\sim 0.15-0.3 \text{ V}$ vs Na/Na⁺ decrease in magnitude over time. As these peaks correspond to the formation and deformation of Na₁₅Sn₄, we believe this transformation is destabilizing, which has been observed in other Sn-based anodes. 43 This could help to explain why the capacity retention is highest in the 1:3 Sn:Sb anode, as the smaller amount of Sn could be less destabilizing for the material upon full sodiation. However, when contrasting the 1:3 Sn:Sb with Sb alone, the Sn could be offering a stabilizing effect at lower potentials during Sb sodiation and desodiation. In an effort to identify mechanical degradation patterns across samples relative to stoichiometry, compositional samples were imaged using SEM after cycling (Fig. S16). Fracturing is observed across all anodes, with the 1:3 Sn: Sb exhibiting some particle agglomeration. Further characterization should be pursued to quantify the extent of fracturing across the different compositions and the influence of the electrolyte on the mechanical properties of the anode.

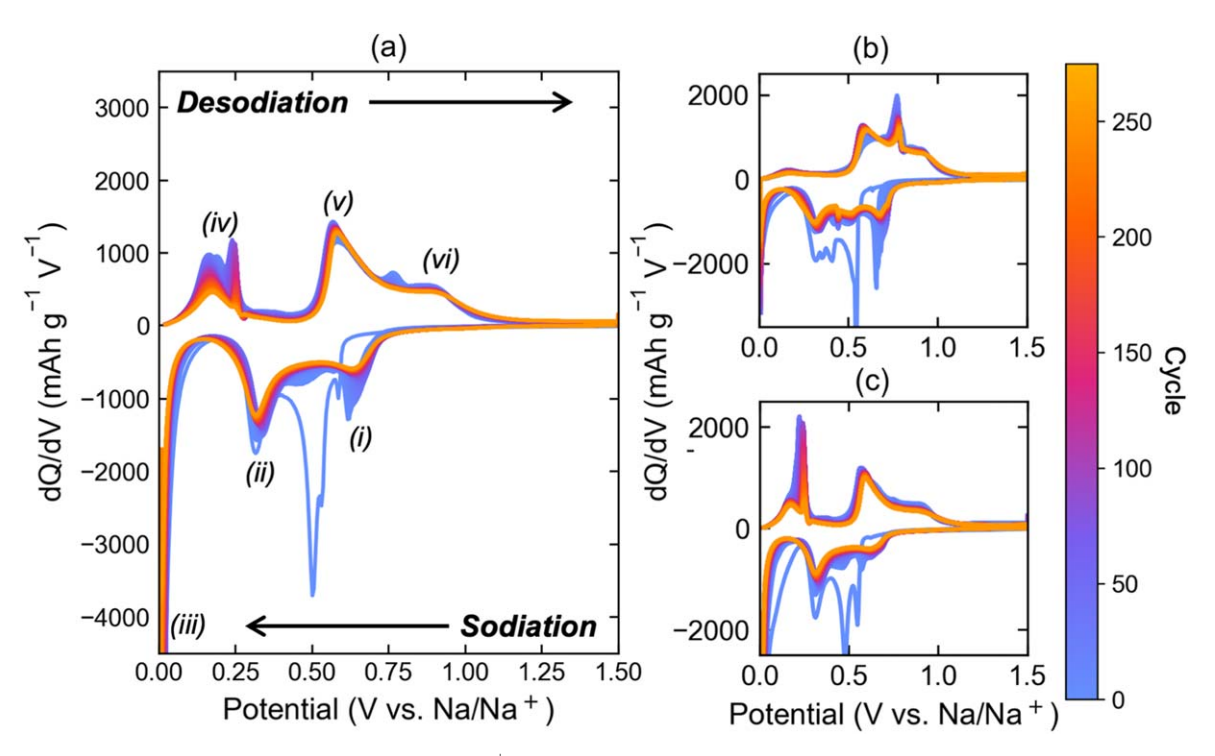


Figure 9. Differential Capacity (dQ/dV) vs potential (V vs Na/Na⁺) of (a) SnSb, (b) 3:1 Sn:Sb, and (c) 1:3 Sn:Sb. alloys in a sodium-ion half-cell. cells were cycled at 0.5 C for 275 cycles. Hypothetical reactions for SnSb are denoted with Roman numerals corresponding to reaction equations detailed in text.

Conclusions

Here, SnSb and Sn-Sb alloys were electrodeposited from ethaline. We identified that the viscous nature of ethaline was inhibiting electrodeposition, so we focused our studies on increasing ionic conductivity. It was found that electrodepositing SnSb at elevated temperatures (between 50 and 80 °C) was effective in electrodepositing crystalline SnSb, so this method was used for increasing ionic conductivity. Water was found to be detrimental to SnSb electrodeposition from ethaline, as films electrodeposited from ethaline with water added were dendritic and did not adhere well to the substrate. After synthesis parameters were optimized samples of SnSb, Sn, Sb, Sn-rich and Sb-rich SnSb were then deposited and cycled in sodium half-cells, which were compared to samples of 1:1 SnSb, and Sn and Sb alone. The sample with 1:3 Sn:Sb retained the highest specific capacity after 275 cycles, followed by Sb. Many factors could be responsible for the increased capacity retention exhibited in the 1:3 Sn:Sb anode, including the smaller grain size and homogeneity of the film relative to the more Sn-rich compositions, or mechanical factors of Sn and Sb sodiation mechanisms. From here, future work should include studying the kinetic limitations of SnSb and studying SEI formation in Sn-Sb anodes.

Additionally, the role of the chosen electrolyte cannot be dismissed. It has been well established that for high energy anodes. where volume expansion remains a critical factor in storage capacity, the solid electrolyte interphase plays a critical role in secondary battery longevity. 44–47 For instance, Sn has shown to operate with greater capacity retention in glyme-based electrolytes compared to carbonate electrolytes.^{8,40,48} However, this is not the case for antimony, which exhibits poor capacity retention in glyme-based electrolytes. 40,49 Finding an optimized electrolyte for Sn-Sb alloy anodes is crucial for not only the optimization of this electrode, but to better understand how the composition of Sn-Sb anodes influence solid electrolyte interphase formation in chosen electrolytes.

Acknowledgments

The authors wish to thank Dr. Amanda Kale for her help with Rietveld Refinements, as well as the Analytical Resources Core (RRID: SCR 021758) at Colorado State University for instrument access, training, and assistance with sample analysis. This work was funded by NSF SSMC-2211067.

ORCID

Jessica R. Gallawa https://orcid.org/0000-0002-5477-6424 Amy L. Prieto https://orcid.org/0000-0001-9235-185X

References

1. J. A. Jorgenson, W. Frazier, P. Denholm, and N. Blair, Grid Operational Impacts of Widespread Storage Deployment (National Renewable Energy Laboratory, Golden, CO) (2022), p. NREL/TP-6A40-80688.

- 2. Y. Tian et al., Chem. Rev., 121, 1623 (2021).
- 3. H. Moriwake, A. Kuwabara, C. A. J. Fisher, and Y. Ikuhara, RSC Adv., 7, 36550
- 4. J. Deng, W. B. Luo, S. L. Chou, H. K. Liu, and S. X. Dou, Adv. Energy Mater., 8, 1701428 (2018).
- 5. H. S. Hirsh et al., Adv. Energy Mater., 10, 2001274 (2020).
- W. T. Jing, C. C. Yang, and Q. Jiang, J. Mater. Chem. A, 8, 2913 (2020).
 J. He, Y. Wei, T. Zhai, and H. Li, Mater. Chem. Front., 2, 437 (2018).
- 8. B. Zhang et al., Adv. Mater., 28, 9824 (2016).
- 9. W. P. Kalisvaart, H. Xie, B. C. Olsen, E. J. Luber, and J. M. Buriak, ACS Appl. Energy Mater., 2, 5133 (2019).
- 10. W. Brehm, J. R. Buchheim, and P. Adelhelm, Energy Technology, 7, 1900389 (2019).
- 11. Z. Yi et al., J. Power Sources, 342, 861 (2017).
- 12. J. S. Gutiérrez-Kolar et al., ACS Appl. Energy Mater., 2, 3578 (2019).
- 13. Z. Yuan et al., ACS Appl. Nano Mater., 4, 826 (2021).
- 14. M. Walter, S. Doswald, and M. V. Kovalenko, J. Mater. Chem. A, 4, 7053 (2016).
- 15. Z. Song, G. Wang, Y. Chen, Y. Lu, and Z. Wen, Chem. Eng. J., 463, 142289 (2023).
- 16. H. Jia et al., ACS Appl. Mater. Interfaces, 10, 9696 (2018).
- 17. S. Jena et al., J. Alloys Compd., 854, 157238 (2021).
- 18. J.-H. Choi, C.-W. Ha, H.-Y. Choi, and S.-M. Lee, J. Ind. Eng. Chem., 60, 451 (2018)
- 19. C. Chen et al., RSC Adv., 5, 30793 (2015).
- 20. H. Xie et al., ACS Energy Lett., 3, 1670 (2018).
- 21. W. Ma et al., Nano Energy, 54, 349 (2018).
- 22. L. Baggetto et al., J. Power Sources, 267, 329 (2014).
- 23. K. Shiva, H. B. Rajendra, and A. J. Bhattacharyya, ChemPlusChem, 80, 516 (2015).
- 24. K. Nieto, N. J. Gimble, L. J. Rudolph, A. R. Kale, and A. L. Prieto, J. Electrochem. Soc., 169, 050537 (2022).
- 25. K. Nieto et al., J. Phys. Chem. C, 127, 12415 (2023).
- 26. J. Ma and A. L. Prieto, Chem. Commun., 55, 6938 (2019).
- 27. E. L. Smith, A. P. Abbott, and K. S. Ryder, Chem. Rev., 114, 11060 (2014).
- 28. S. Kaur, A. Malik, and H. K. Kashyap, J. Phys. Chem. B, 123, 8291 (2019).
- 29. L. F. Audrieth and H. W. Nelson, Chem. Rev., 8, 335 (1931).
- 30. A. P. Abbott, R. C. Harris, and K. S. Ryder, J. Phys. Chem. B, 111, 4910 (2007).
- 31. Y. Zhang et al., J. Phys. Chem. B, 124, 5251 (2020).
- 32. A. P. Abbott et al., *Electrochim. Acta*, 176, 718 (2015).
- 33. L. Fathyunes and J. Khalil-Allafi, Ultrason. Sonochem., 42, 293 (2018).
- 34. C. Sun, J. Zeng, H. Lei, W. Yang, and Q. Zhang, ACS Sustain. Chem. Eng., 7, 1529 (2019).
- 35. X. Shen, N. Sinclair, J. Wainright, R. Akolkar, and R. F. Savinell, J. Electrochem. Soc., 167, 086509 (2020).
- 36. I. Alfurayj et al., J. Phys. Chem. B, 125, 8888 (2021).
- 37. J. R. Brusas and E. M. B. Dela Pena, J. Electrochem. Sci. Technol., 12, 387 (2021).
- 38. X.-Z. C. Hao, 28, 2103071 (2022).
- 39. A. T. S. C. Brandão et al., Coatings, 9, 798 (2019).
- 40. B. Qin et al., ACS Appl. Mater. Interfaces, 12, 3697 (2020). 41. M. Fehse et al., J. Mater. Chem. A, 6, 8724 (2018).
- 42. A. Darwiche, M. T. Sougrati, B. Fraisse, L. Stievano, and L. Monconduit, Electrochem. Commun., 32, 18 (2013).
 43. T. Li et al., ACS Appl. Energy Mater., 2, 860 (2019).
 44. X. Du, Y. Gao, and B. Zhang, Adv. Funct. Mater., 31, 2102562 (2021).

- 45. E. Olsson et al., *Small*, **18**(43), e2200177 (2022).
- 46. Y. Gao and B. Zhang, "Probing the Mechanically Stable Solid Electrolyte Interphase and the Implications in Design Strategies." Adv. Mater., 35, 2205421 (2023).
- 47. U. S. Meda, L. Lal, S. M, and P. Garg, Journal of Energy Storage, 47, 103564 (2022).
- 48. J. Huang et al., Energy Environ. Sci., 12, 1550 (2019).
- 49. K. Pfeifer et al., ChemElectroChem, 7, 3487 (2020).